

## Selective adsorption of acidic gases from ternary mixture by acetate- and sulfonate-based ionic liquids at molecular level

Sadiye VELİOĞLU\* 

Gebze Technical University, Institute of Nanotechnology, Kocaeli, Turkey

Received: 19.03.2021 • Accepted/Published Online: 30.09.2021 • Final Version: 23.02.2022

**Abstract:** This paper attempts to elucidate the competitive adsorption mechanism of thin films of ionic liquids (ILs) on the surface of porous materials for acidic gases at a molecular level in order to design a proper material for the diminishment of gas emissions. Thin film 1-butyl-3-methylimidazolium ([BMIM]<sup>+</sup>) cation-based IL systems composed of four different anions such as [CH<sub>3</sub>CO<sub>2</sub>]<sup>-</sup> and [CF<sub>3</sub>CO<sub>2</sub>]<sup>-</sup> (acetate-based), and [CH<sub>3</sub>SO<sub>3</sub>]<sup>-</sup> and [CF<sub>3</sub>SO<sub>3</sub>]<sup>-</sup> (sulfonate-based) are created in contact with the gas phase containing ternary H<sub>2</sub>S/CO<sub>2</sub>/CH<sub>4</sub>:1/25/74 mixture. To define gas adsorption performance at gas-liquid interface and bulk liquid phase, classical molecular dynamics simulations are carried out. Adsorption of acidic gases is governed by the formation of an adsorbed gas layer on the surface of the ionic liquid based on thermodynamics aspects, and then the partial dissolution of gases in the bulk liquid phase is accompanied by the transport of gases. These behaviors are followed by several analysis methods in simulation approaches such as radial distribution function (RDF) of gases around specific atoms of ILs, lateral displacement of gas molecules, radial distance between gas and ILs, interaction energy between gases and ILs, and average number of hydrogen bonding between ions with and without adsorbed gases. Acetate-based ILs performed twice as good in CO<sub>2</sub> adsorption capacity than sulfonate-based ILs. However, the one having -CF<sub>3</sub> group in acetate-based ILs has short CO<sub>2</sub> retention time and high CH<sub>4</sub> adsorption capacity, diminishing the H<sub>2</sub>S+CO<sub>2</sub>/CH<sub>4</sub> adsorption selectivity. High CO<sub>2</sub> adsorption performance of acetate-based ILs is related to their strong anion-cation interaction and less hydrogen-bonding ability between cation tail and anion, which is the source for free space between anion and cation. Those with high adsorption capacities and long retention times are those that can ensure that CO<sub>2</sub> molecules are coordinated in these free volumes between cation tails and anions. Therefore, here, the effect of different parameters on the CO<sub>2</sub> and H<sub>2</sub>S adsorption over CH<sub>4</sub> is revealed via atomistic design, and the importance of selection of suitable anions in IL for identifying potential nanocomposite adsorbent materials for acidic gas removal is highlighted.

**Key words:** CO<sub>2</sub> and H<sub>2</sub>S adsorption, ionic liquids, molecular dynamics simulations, adsorption mechanism

### 1. Introduction

The global climate warming threatens ever-increasingly countries all around the world, which originates from the emission of greenhouse gases. Its consequences are started to damage our living environment and hinder economic development. Carbon dioxide (CO<sub>2</sub>) is the main responsible gas for the frightening state of affairs with its concentration in the atmosphere around 400 ppm [1]. Hydrogen sulfide (H<sub>2</sub>S) is the other acidic gas that threatens the environment and human health. The emission of these acidic gases will be inevitable as long as we continue to use petroleum, coal, and natural gas as primary global fuels. Additionally, natural sources such as volcanoes, natural gas wells, and sulfur springs, and industrial activities are the other sources for H<sub>2</sub>S. Therefore, CO<sub>2</sub> and H<sub>2</sub>S storage and capture from fuels by chemical and physical absorption and adsorption processes, or the combination of the features of absorbents and adsorbent processes are highly appreciated due to their help in diminishing the acidic gas load in the atmosphere with low energy penalty [2]. Therefore, for their mutual contributions, composite materials were produced by the incorporation of ionic liquid (IL) having permanent porosity into the porous solid adsorbent such as metal organic framework (MOF), covalent organic framework (COF), zeolite, etc. [3-4]. In this sense, superior acidic gas adsorption performance of ILs from biogas had led their widespread use in several separation processes by the impregnation in nanoporous solids, which is accepted as a promising strategy to design new surface properties within porous materials for gas adsorption [5-8].

ILs composed of large asymmetric organic cations and smaller inorganic or organic anions are considered as green solvents due to their negligible vapor pressure and enhanced physical and chemical stability [9]. Their favorable solvation

\* Correspondence: sadiyevelioglu@gtu.edu.tr

properties gained considerable attention in the processes of CO<sub>2</sub> and H<sub>2</sub>S storage and capture. Since cation and anion of IL can be tailored, its physicochemical properties can be readily modified to optimize acidic gas absorption/adsorption performance. After the first discovery of CO<sub>2</sub> adsorption capacity of imidazolium-based ILs by Blanchard et al. [10], they were started to be tested by several experimental and theoretical studies such as gravimetric microbalance [11], the synthetic (bubble point) method [12], and isochoric saturation [13] in experimental measurements as well as molecular dynamics (MD) [14], Monte Carlo (MC) [15], and quantum mechanical (QM) [16] simulations in theoretical computations. Since it was well-established that imidazolium-based ILs have high CO<sub>2</sub> and H<sub>2</sub>S adsorption performances, their most suitable combinations with anions were intensely investigated. Within the hundreds of different anions, high acidic gas solubilities of acetate-based ILs [17–19] corresponding to their potential of formation of chemical bonds, and sulfonate-based ILs [20–22] at high pressures were revealed in the literature.

To further improve the separation properties of nanoporous materials, which are used as adsorbents, studies were concentrated on the impregnation of ILs into these porous materials. Mohamedali et al. reported an increase of 700 % for the [BMIM]<sup>+</sup>[Ac]<sup>-</sup>@ZIF-8 with 30 wt.% IL loading [5] and 200 % for [BMIM]<sup>+</sup>[Ac]<sup>-</sup>@HKUST-1 with 5 wt.% IL loading [6] in CO<sub>2</sub> adsorption capacity compared to pristine MOFs at 303 K and 0.15 bar. Shahrom et al. [7] revealed that CO<sub>2</sub> adsorption capacity of [DMEDAH]<sup>+</sup>[Ac]<sup>-</sup>@activated carbon (AC) enhanced from 0.08 mmol/g (pure AC) to 0.77, 0.87, and 0.36 mmol/g with 10, 20, and 30 wt.% IL loadings at 298 K and 1 bar. Similarly, Liu et al. [8] reported 80% improvement in CO<sub>2</sub> adsorption capacities of polyetherimide (PEI)/SBA-15 composites with the impregnation of [EMIM]<sup>+</sup>[Ac]<sup>-</sup> (from 1.18 to 2.20 mmol/g) at 303 K.

Considering high adsorption capacities of acetate- and sulfonate-based ILs for acidic gases, and their outstanding adsorption-based separation performances as impregnated into porous solids, the investigation of adsorption capacities of pristine acetate- and sulfonate-based ILs for the ternary mixture of CO<sub>2</sub>, H<sub>2</sub>S, and CH<sub>4</sub> is emerged due to the determination of their actual performance. Since especially, the selective adsorption of H<sub>2</sub>S and CO<sub>2</sub> from CH<sub>4</sub> by ILs impregnated into different solid and polymeric materials is of great significance, it is required initially to understand the structure-property relationship of pristine ILs for acidic gas separation. Moreover, since there is a high demand on the identification of more realistic performance of adsorbents, we investigated H<sub>2</sub>S/CO<sub>2</sub>/CH<sub>4</sub> ternary mixture separation by acetate- and sulfonate-based IL adsorbents. The most feasible and cost-effective way to carry out this analysis is to perform theoretical investigations using molecular dynamics simulations. Therefore, it is aimed in this study to scrutinize the adsorption mechanism of acetate- and sulfonate-based ILs for acidic gases in ternary mixture using molecular dynamics simulations. Four ILs consisting of same cation as 1-butyl-3-methylimidazolium [BMIM]<sup>+</sup> and different anions such as alkylsulfonate [CH<sub>3</sub>SO<sub>3</sub>]<sup>-</sup> (ASF), triflate [CF<sub>3</sub>SO<sub>3</sub>]<sup>-</sup> (OTF), acetate [CH<sub>3</sub>CO<sub>2</sub>]<sup>-</sup> (OAC), trifluoroacetate [CF<sub>3</sub>CO<sub>2</sub>]<sup>-</sup> (TFA) are selected. The composition of ternary H<sub>2</sub>S/CO<sub>2</sub>/CH<sub>4</sub>:1/25/74 mixture was set following the acid gas content in raw natural gas streams, which vary according to the source, commonly in the range of 25–55 mol.% for CO<sub>2</sub> and below 2 mol.% for H<sub>2</sub>S [23]. Since the highest CH<sub>4</sub> concentration in the bulk phase will reduce the total adsorbed amount of CO<sub>2</sub> and CH<sub>4</sub> on any adsorbent material [24], the lowest content of CO<sub>2</sub> (or highest content of CH<sub>4</sub>) is preferred in order to reveal the adsorption capacities of the selected ILs at the harsh conditions. It is worth to note that at high CO<sub>2</sub> content or at high pressure, the adsorbed CO<sub>2</sub> amount will increase.

## 2. Computational details

Theoretical investigation is carried out using molecular dynamics simulations via Large-scale Atomic/Molecular Massively Parallel Simulator (LAMMPS) [25] open source software. Visual Molecular Dynamics (VMD) package [26] is used for the visualization of designed systems and post-analysis. For the ionic liquids (ILs) depicted in Figure 1, OPLS-AA [27] force field is used, but specific parameters developed by Lopes et al. [28-29] are adapted to encompass the entire homologous series of IL. A three-site rigid molecule with Lennard-Jones (LJ) 12-6 potential is used to model both CO<sub>2</sub> [30] and H<sub>2</sub>S [31] and locations of partial point charges are set at the center of each side, as given in Table 1. Single-site spherical LJ 12-6 potential is used for CH<sub>4</sub> [32] molecules. Long-range electrostatic interactions are treated with the PPPM Ewald method. Bond distances involving hydrogen atoms in IL are constrained using the SHAKE algorithm. The cut-off distance for non-bonded interactions is adjusted as 18 Å. The cross-term parameters for interaction between i and j atoms are calculated as  $\epsilon_{ij}=(\epsilon_{ii}\times\epsilon_{jj})^{1/2}$  and  $\sigma_{ij}=(\sigma_{ii}+\sigma_{jj})/2$ .

Figure 2 represents the initial state of one of the investigated simulation system containing IL film exposed to gas phase. As an example, the initial and final configurations of system of [BMIM]<sup>+</sup>[CH<sub>3</sub>CO<sub>2</sub>]<sup>-</sup> are given in Figure 2 (a) and (b). Each system includes 500 ion pairs (namely, 500 anions and 500 cations) that constitute an IL layer of approximately 40 Å thicknesses along the x-axis. Initial configurations of systems including bulk IL layer and gas phase are randomly generated using the Packmol software [33]. Ion pairs consisting of IL are centered in the middle of unit-cell and surrounded with

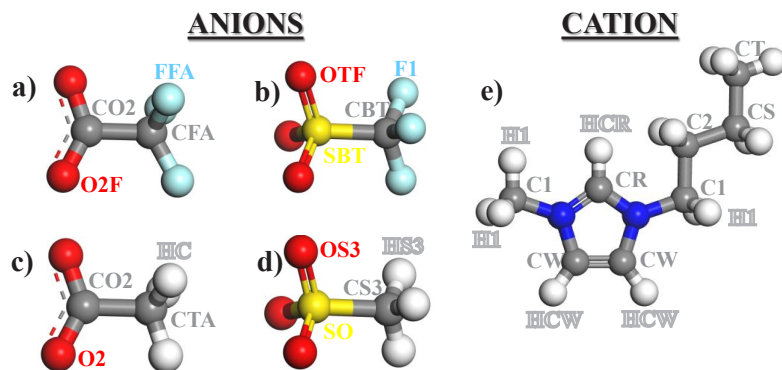


**Figure 1.** Molecular representation of anions such as (a) trifluoroacetate (TFA), (b) triflate (OTF), (c) Acetate (OAC), and (d) alkylsulfonate (ASF), and 1-butyl-3-methylimidazolium ([BMIM]<sup>+</sup>) cation with atomic site labels on each molecule. Note that hydrogen atoms having missing atomic sites in cation are labeled as HC.

**Table 1.** Potentials used for gas molecules in molecular simulations.

Gas molecule	Atom	$\epsilon$ (K)	$\sigma$ (Å)	$q$ (e)
CO <sub>2</sub>	C	27.0	2.80	0.70
	O	79.0	3.05	-0.35
H <sub>2</sub> S	H	3.9	0.98	0.124
	S	250	3.72	-0.248
CH <sub>4</sub>	single sphere	148.0	3.73	0.00

gas phases at both ends along the x-axis. The area of the IL surface contacting with the gas phase is about  $64 \times 64 \text{ \AA}^2$  (a side lengths of y- and x-axes), which is enough to observe a reliable statistic for the estimation of surface adsorption and interface region between IL and gas phases. Total thickness of gas phase along the x-axis is set to approximately 80 Å, including 2, 50, and 148 molecules of H<sub>2</sub>S, CO<sub>2</sub>, and CH<sub>4</sub>, respectively, which corresponds to the composition of the ternary H<sub>2</sub>S/CO<sub>2</sub>/CH<sub>4</sub>:1/25/74 mixture. Periodic boundary conditions are applied to each direction of simulation unit-cell.

First of all, initial configurations of ILs are allowed to relax with zero-temperature minimizations for 1 ns, followed by gradually increase to 500 K using NpT (iso-baric iso-thermal ensemble) runs for 5 ns, after which the temperature is gradually decreased to 298 within 2 ns. Subsequently, NpT run along 2 ns is performed at 298 K to equilibrate the system. Then, pre-equilibrated IL phase at 298 K is further used to generate a system such as that displayed in Figure 2 (a) by extending the length of unit-cell in x-direction and randomly distributing the gas molecules into this created vacuum phase to observe gas phase. Finally, in order to observe the equilibrated gas-IL interface, each system is relaxed using NVT (canonical ensemble) run for 5 ns at 298 K and 1 bar. For the sampling, further 15 ns NVT run is performed at the same conditions. For comparison, in each system, temperature is maintained at 298 K by the Nosé–Hoover thermostat with a coupling time constant of 100 fs, and pressure is maintained at 1 bar by the Nosé–Hoover barostat with a coupling time constant of 500 fs. The simulation time step is set to 1 fs. Figure 2 (b) displays the final state of well-equilibrated [BMIM]<sup>+</sup>[CH<sub>3</sub>CO<sub>2</sub>]<sup>-</sup>, which is observed after 5 ns of equilibration and 15 ns of sampling, revealing gas and IL phases and gas-IL interfaces, which is displayed with the two dashed lines.

Once the detailed atomistic systems are constructed, the conformational characteristics, namely, radial distribution function (RDF), interaction energy, and number of hydrogen-bonding (h-bonding) between each molecule types are estimated. The number of gas molecules within bulk IL layer and gas-IL interface, and distance between CO<sub>2</sub> and specific groups on IL are calculated along the simulation time. Both density distribution and map of gases are provided to elucidate the adsorption mechanism of each IL for each gas. Finally, displacement of CO<sub>2</sub> molecules adsorbed in the bulk of IL is provided by 3D maps.

The RDF ( $g(r)$ ) gives the probability of finding a given pair at defined distance compared with the average probability according to Equation 1.

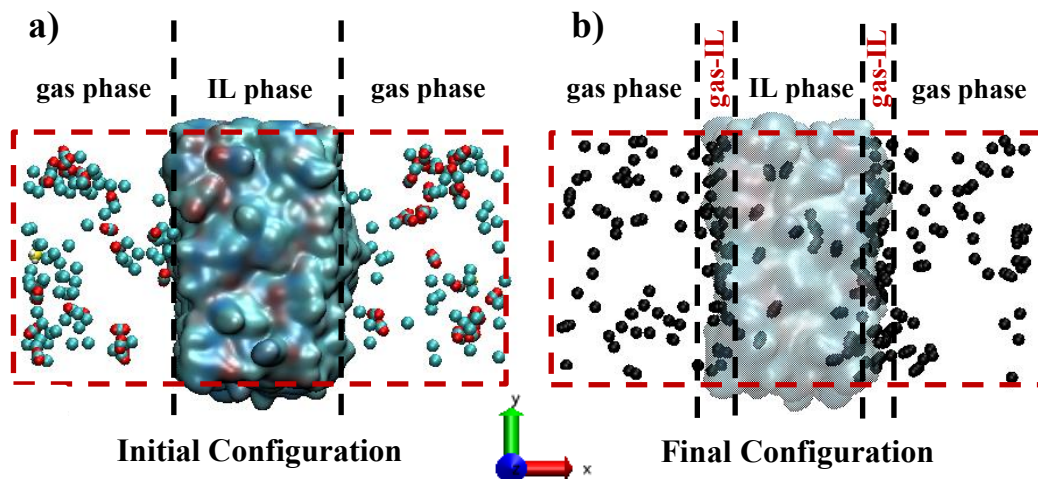


**Figure 2.** Representation of (a) initial and (b) final states of  $[\text{BMIM}]^+[\text{CH}_3\text{CO}_2]^-$  system consisting of 500 ion pairs. Please note that randomly packed  $\text{H}_2\text{S}$ ,  $\text{CO}_2$ , and  $\text{CH}_4$  molecules in (a) are represented with yellow, red and cyan colors, and all gas molecules in (b) are illustrated with black.

$$g_{ij}(r) = \frac{\Delta N_{ij}(r, r + \Delta r)}{4\pi r^2 \Delta r N_i N_j} \quad (1)$$

where  $r$  is the distance between species  $i$  and  $j$ ,  $\Delta N_{ij}(r, r + \Delta r)$  is the number of species  $j$  around  $i$  within a shell from  $r$  to  $r + \Delta r$  as given in Figure 3,  $N_i$  and  $N_j$  are the numbers of species  $i$  and  $j$ . According to the location and intensity of the peaks in the RDF, for instance, we can define the distribution of gas molecules around anion or cation of ILs.

H-bonding is defined based on the oxygen atoms in the anion of IL and carbon atoms in the cation of IL both in the presence and absence of gas molecules in the bulk IL phase. The applied criterion for h-bonding is that the distance between the donor and acceptor atoms is less than  $3.2 \text{ \AA}$  and the angle of the  $\text{C-H}\cdots\text{O}$  bond is greater than  $130^\circ$ . Although it was well-demonstrated that the anion tends to orientate close to CR atom type (see Figure 1) in  $[\text{BMIM}]^+$  cation by creating h-bonding in the bulk IL phase [34], the numbers of h-bonding between anion and CW, C1, and CT atom types in the cation are also investigated.

The average interaction energy between defined pairs is extracted over simulation time to quantitatively investigate the interaction phenomena. Only inter-molecular (non-bonded) potential energy is involved in the interaction energy and averaged over time by 15 ns of the sampling for each IL system. The electrostatic interactions are modeled by the Coulombic potential using Equation 2, where the energy of the interaction is inversely proportional to the distance of separation  $r_{ij}$ :

$$E_{\text{Coul.}} = \frac{e^2}{4\pi\epsilon_0} \sum_{i \neq j} \frac{q_i q_j}{r_{ij}} \quad (2)$$

The partial charges  $q_i$  and  $q_j$  are derived from quantum mechanics calculations,  $e$  is the charge of the electron, and  $\epsilon_0$  is the dielectric permittivity of vacuum. Dispersive interactions are modeled with a 12-6 LJ potential with Equation 3:

$$E_{\text{LJ}} = \sum_{i \neq j} \epsilon_{ij} \left[ \left( \frac{\sigma_{ij}}{r_{ij}} \right)^{12} - 2 \left( \frac{\sigma_{ij}}{r_{ij}} \right)^6 \right] \quad (3)$$

$\epsilon_{ij}$  is the depth of the potential well, and  $\sigma_{ij}$  is the finite distance at which the inter-particle potential is zero, and they are empirical parameters derived from the fitting of the model to observed structural and physical property data.

Mass density profiles of each gas molecules, cation and anions, are computed for each chunk having  $0.2 \text{ \AA}$  size (i.e. total-mass/volume) along the x-axis from the 15-ns sampling. Each system is split into uniform chunks perpendicular to the interface normal, and one-dimensional local density in each chunk along the x-axis of unit-cell is calculated in unit of molecule/ $\text{\AA}^3$  as following:

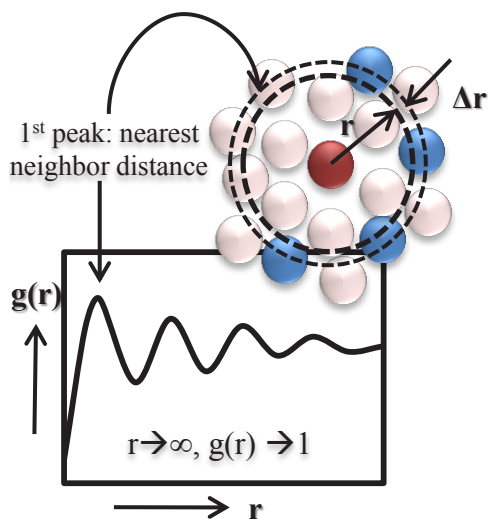


Figure 3. Schematic illustration of  $g(r)$  dependence on distance ( $r$ ).

$$\rho(x) = \frac{1}{A_0} \sum_{i=0}^N \delta(x-x_i) \quad (4)$$

where  $\rho(x)$  is the global density profile,  $A_0$  is the nominal cross sectional area,  $N$  is the number of atoms,  $x_i$  is an atom coordinate along the axis perpendicular to the interface.

### 3. Results and discussion

#### 3.1. Comparison of gas adsorption in each IL system

To study the effect of pure ILs on acidic gas adsorption of bulk IL phase, number of adsorbed gas molecules varied within 15-ns simulation time is identified as given in Figures 4 (a-d). Since high  $\text{CO}_2$  and  $\text{H}_2\text{S}$  and less  $\text{CH}_4$  uptakes are desirable for the design of adsorbent material, initially the performance of ILs for  $\text{CO}_2$  and  $\text{H}_2\text{S}$  are examined. Acetate-based ILs display higher  $\text{CO}_2$  adsorption capacity, almost double compared to the sulfonate-based ILs. However, when the adsorption rate of  $\text{CO}_2$  within 15-ns is considered, it can be seen that either acetate- or sulfonate-based ILs having  $-\text{CH}_3$  functional groups (ASF and OAC) reveal the frequent  $\text{CO}_2$  adsorption within 1-2 ns of their contact. But the ones having  $-\text{CF}_3$  functional groups display slow  $\text{CO}_2$  adsorption rate and large scattering in the number of adsorbed gas within the simulation time. On the other hand, it is not easy to provide similar conclusion when  $\text{H}_2\text{S}$  adsorption of ILs is considered, where it follows the order of  $\text{ASF} > \text{OAC} \approx \text{OTF} \gg \text{TFA}$ . Since  $\text{H}_2\text{S}$  adsorption of ASF is greater than the rest, it reveals highest  $\text{H}_2\text{S}/\text{CH}_4$  adsorption selectivity. However, when  $\text{CO}_2/\text{CH}_4$  selectivity of ASF is considered and the total acidic gas selectivity ( $\text{H}_2\text{S}+\text{CO}_2/\text{CH}_4$ ) is calculated, OAC takes the first place as shown in Figure 4 (e). Adsorption selectivity of OTF is the lowest due to having twice as much as  $\text{CH}_4$  adsorption compared to other ILs. Collectively, considering acidic gas separation performances, OAC is the best candidate within the investigated ILs with high adsorption capacity and rapid adsorption rate as well as adsorption selectivities of 17, 21, and 17 for  $\text{CO}_2/\text{CH}_4$ ,  $\text{H}_2\text{S}/\text{CH}_4$ , and  $\text{H}_2\text{S}+\text{CO}_2/\text{CH}_4$ , respectively. Finally, average numbers of adsorbed  $\text{CO}_2$  and  $\text{CH}_4$  molecules on both gas-IL interfaces (see Figure 2 (b)), whose thickness are varied between 6 and 8 Å, are given in Figure 4 (f). Although average number of  $\text{CO}_2$  located on the interface is almost same for the investigated ILs, there is a difference for those of  $\text{CH}_4$ , even though not obvious. Highest  $\text{CH}_4$  adsorption of OTF in the bulk IL phase is evidently related to its high  $\text{CH}_4$  adsorption capacity on gas-IL interface. This result unfortunately hinders the adsorption selectivity of OTF and its potential use for acidic gas separation.

To reveal the mobility of adsorbed  $\text{CO}_2$  molecules into the IL phase, displacements of few  $\text{CO}_2$  molecules are illustrated by 3D maps in Figure 5 (a). The findings provided in Figures 4 (a-d) are also verified by Figure 5 (a) that adsorbed  $\text{CO}_2$  molecule on the surface of either ASF or OAC phases instantly prefers to move through the middle of bulk IL phase and keep trapped there. For OTF and TFA ILs, delay for the further move of  $\text{CO}_2$  through the IL bulk phase is yielded  $\text{CO}_2$  to hover over the gas-IL interface. After these adsorbed  $\text{CO}_2$  molecules diffused through the bulk IL phase, they revealed large displacement within the simulation time inside bulk OTF and TFA phases. However, the ones adsorbed by ASF and

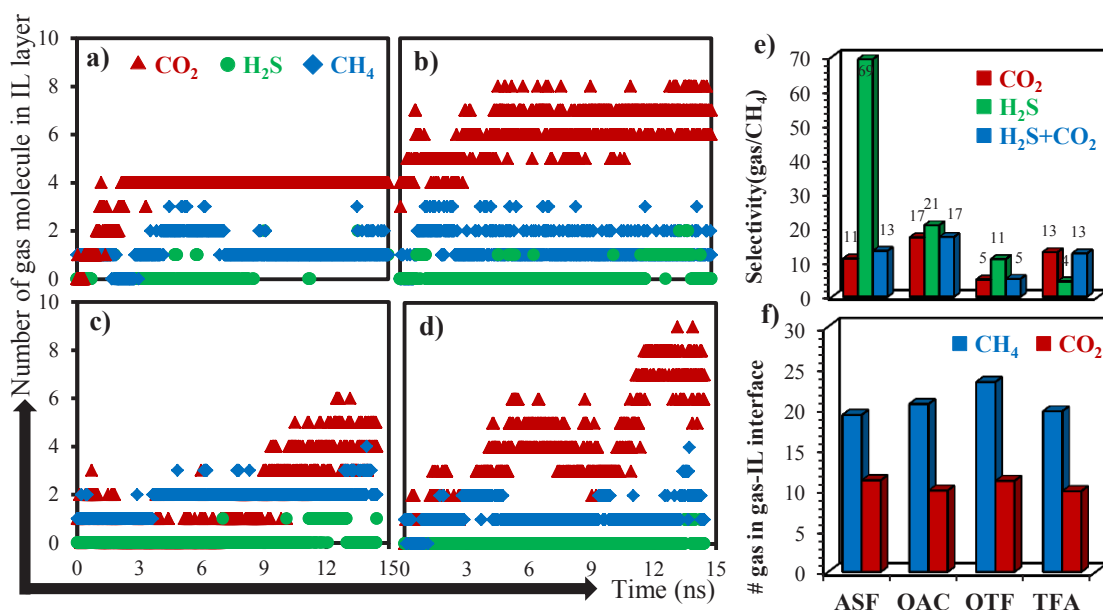


**Figure 4.** Adsorption performances of ILs for acidic gases from natural gas. Number of adsorbed gas molecules varied over 15-ns simulation time in the bulk phase of (a) ASF, (b) OAC, (c) OTF, and (d) TFA ionic liquids. (e) Adsorption selectivities of ILs for CO<sub>2</sub>/CH<sub>4</sub>, H<sub>2</sub>S/CH<sub>4</sub>, and H<sub>2</sub>S+CO<sub>2</sub>/CH<sub>4</sub> mixtures, calculated using the average number of adsorbed gas molecules into the bulk phase of ILs within simulation time. (f) Average number of adsorbed CO<sub>2</sub> and CH<sub>4</sub> molecules on the gas-IL interfaces within simulation time by ILs.

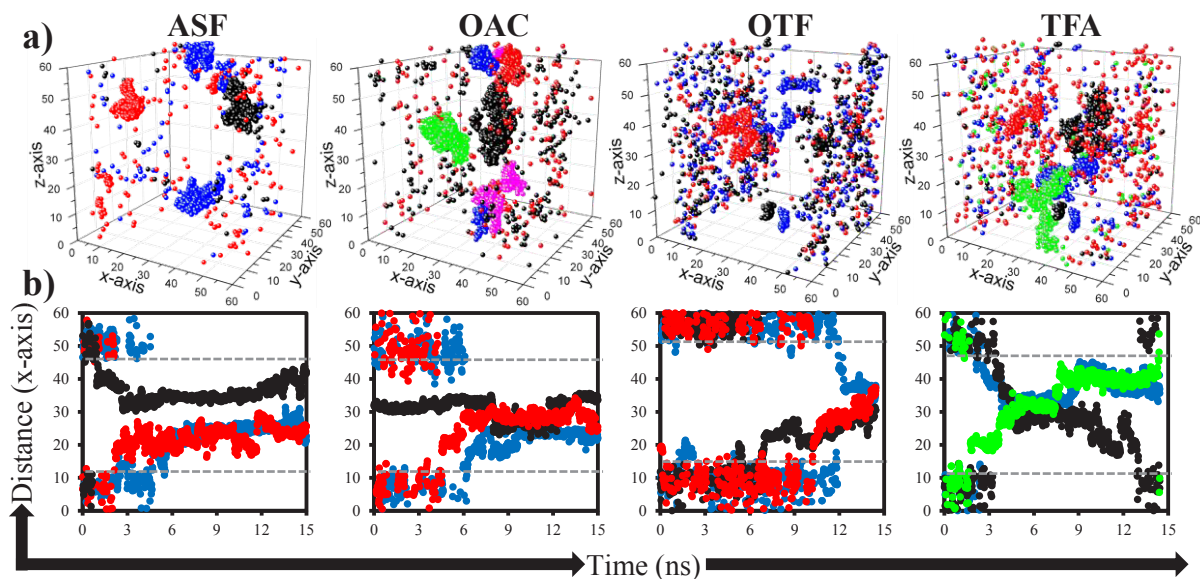


**Figure 5.** (a) Displacement of adsorbed CO<sub>2</sub> molecules within the bulk IL phase along x-, y-, and z-axes. (b) Displacement of three adsorbed CO<sub>2</sub> molecules, identified in (a) with the same color, along x-axis within 15-ns simulation time. Three, five, three, and four numbers of CO<sub>2</sub> molecules are provided in (a) for ASF, OAC, OTF, and TFA, respectively. Grey dashed lines in (b) represents the approximate borders of bulk IL phase.

OAC ILs seem stuck in their location and display very little displacement. When the designed systems are considered (see Figure 2 (a)), IL phase is continuous in y- and z-axes, but finite in x-axis. Therefore, displacement of CO<sub>2</sub> in x-axis from one interface to the other will provide information about the transport of adsorbed gases through IL phase. To reveal CO<sub>2</sub> transport through IL phase, displacements of three CO<sub>2</sub> molecules given in Figure 5 (a) along x-axis are provided in Figure 5 (b). The selected adsorbed three CO<sub>2</sub> molecules are transported very rapidly through the middle of IL phase

within approximately 3 ns for ASF and 6 ns for OAC, and stuck there until the end of simulation time (15 ns). This high adsorption and low transport rate (long retention time) of  $\text{CO}_2$  in OAC was also reported in the study of Aghaie et al. [35] where they compared  $[\text{BMIM}]^+[\text{CH}_3\text{CO}_2]^-$  with  $[\text{EMIM}]^+[\text{BF}_4]^-$ . For OTF, adsorption time of selected  $\text{CO}_2$  molecules is much longer than those of ASF and OAC. However, in addition to high adsorption capacity of TFA for  $\text{CO}_2$ ,  $\text{CO}_2$  transport rate in TFA phase is also greater than the rest of ILs. Two  $\text{CO}_2$  molecules which are adsorbed from one surface of TFA at around 3<sup>rd</sup> ns released from the other surface of TFA at around 14<sup>th</sup> ns. Additionally,  $\text{CO}_2$  molecules are not fixed in the same environment after the adsorbed by TFA, they jump from one region to the other, as illustrated by step-wise change in the displacement of x-axis in Figure 5 (b). Therefore, this shows that retention time of  $\text{CO}_2$  molecules is shorter in TFA, which is the other shortcoming of TFA in acidic gas separation in addition to its less  $\text{H}_2\text{S}$  adsorption.

### 3.2. Structural differences in each IL system induced by $\text{CO}_2$ adsorption

In order to provide a mechanistic understanding of adsorption process induced by ILs, structural differences of IL systems observed after gas adsorption are compared. Orientation of oxygen atoms in anions with respect to the selected atoms in cation (see Figure 1 for atomic site labels) is investigated for each IL using RDF analysis as given in Figure 6 (a). Since the same trend in RDF of each IL is observed between anion and cation, only RDF of OAC is provided in Figure 6 (a). Oxygen atoms of anion dominantly prefer to locate around the carbon atoms in the polar head of cation, where this preference of several different anions to CR type carbon atom of imidazolium cation was supported in the literature [34, 36]. Klahn and Seduraman [37] proposed that  $\text{CO}_2$  adsorption led to reorientations of anions in the IL. However, similar with the data provided in this study, they also could not see any changes in RDFs of cation–anion pair when they compared RDFs observed before and after  $\text{CO}_2$  adsorption [37]. On the other hand, the most preferential adsorption sites of ion pairs for  $\text{CO}_2$  adsorption are displayed in Figure 6 (b) using RDF between  $\text{CO}_2$  and some specific atoms in ions. Again, since the high intensities in the RDFs of  $\text{CO}_2$ –carbon atom in anion (e.g.,  $\text{CO}_2$ –CTA for OAC IL) and  $\text{CO}_2$ –CT (carbon atom in the apolar tail of cation) are observed for all types of ILs, only RDF for OAC is provided. Figure 6 (b) evidently represents that  $\text{CO}_2$  molecules reveal high preference to the carbon atoms on tail of cation, since anions are loosely coordinated around them, as given in Figure 6 (a) with the peak having least intensity for cation (CT)–anion (O2) in OAC IL. Therefore, the RDFs of cation (CT)–anion (O2) in all IL systems observed after  $\text{CO}_2$  adsorption are compared in Figure 6 (c). The highest coordination of cation (CT) around anion (O2) is observed in OAC, and ASF follows it. This observation obviously explains the reason for their long retention time and low displacement of  $\text{CO}_2$  illustrated in Figure 5. Due to the comparably highly orientation of cation (CT) around anion (O2) in OAC and ASF,  $\text{CO}_2$  molecules adsorbed between them are not able to move freely and trapped in the free volume space existing between them, and, hence, cation– $\text{CO}_2$ –anion network dominates.

The environment of adsorbed  $\text{CO}_2$  molecules as visualized in Figure 7 (a) is dominantly consisting of several cation tails and anions. Adsorbed  $\text{CO}_2$  molecules into ASF and OAC ILs are surrounded by almost same number of cations and anions during the simulation time. Only one frame at the end of simulation time is given in Figure 7 (a) which shows that adsorbed  $\text{CO}_2$  molecules into OTF and TFA ILs are surrounded by higher amount of cation tails than anions. This reveals the lack of network of cation– $\text{CO}_2$ –anion, which diminishes the trap of  $\text{CO}_2$  and, hence, enables easily transportation and desorption of  $\text{CO}_2$ . On the other hand, Figures 7 (b-c) display the variation of radial distance between  $\text{CO}_2$  and the selected three cations and anions within simulation time, respectively. Accordingly, randomly selected adsorbed  $\text{CO}_2$  molecules into ASF and OAC do not change their environment within simulation time. When the distance between anion

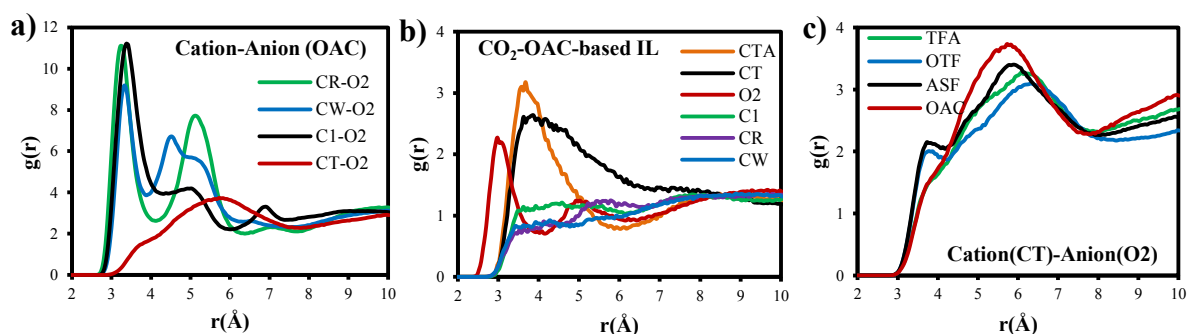


**Figure 6.** Radial density distribution functions between (a) specific atom sites in cation and oxygen in anion, (b)  $\text{CO}_2$  and specific atom sites in cation/anion, and (c) carbon atom of the tail of imidazolium cation and oxygen of the anion in each IL. Please note that (a) and (b) graphs are only provided for OAC IL due to the similarities in trend for other ILs.

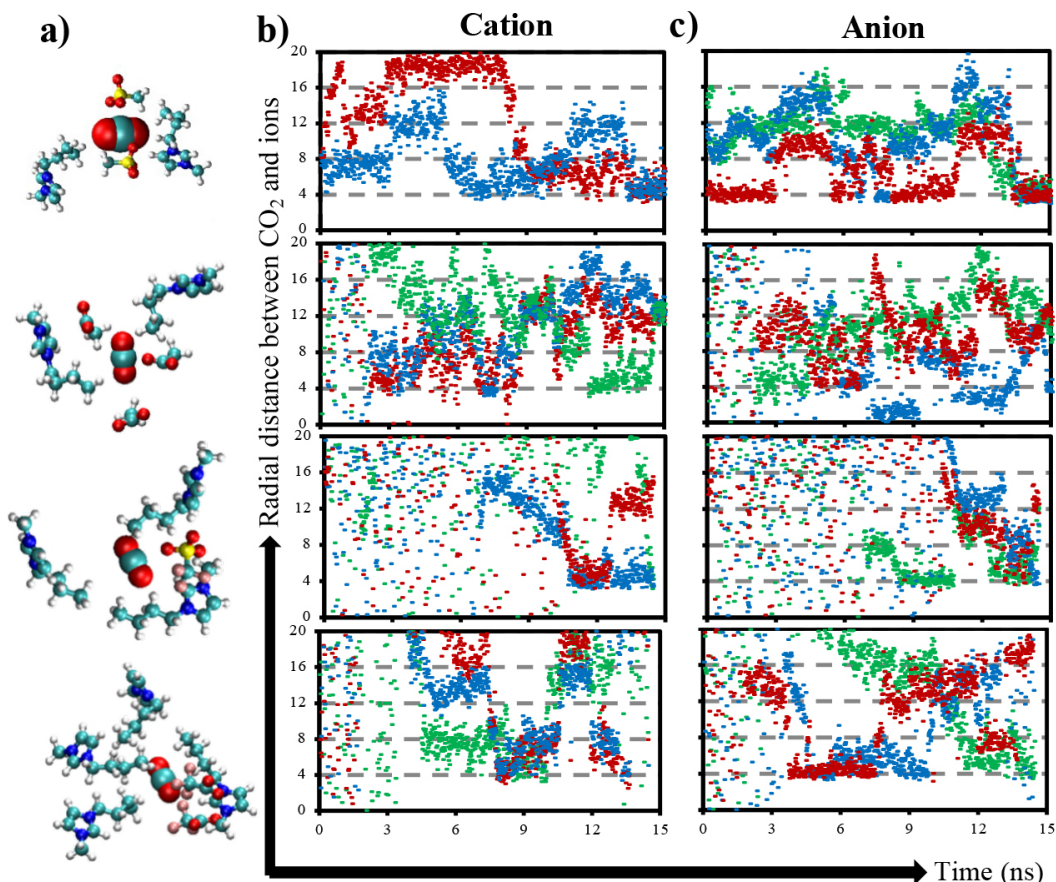


**Figure 7.** (a) Cation and anion orientations around one of the adsorbed CO<sub>2</sub> molecule, where snapshots are taken from the last frame of 15-ns trajectory. Variation of radial distance between (b) randomly selected carbon atoms (CT) in the tail of cation and CO<sub>2</sub> molecules, and (c) oxygen atoms of anion and CO<sub>2</sub> molecules within 15-ns simulation time. Please note that from top to down, data belong to the ASF, OAC, OTF, and TFA, respectively.

and CO<sub>2</sub> (Figure 7 (c)) is compared with that of between tail of cation and CO<sub>2</sub> (Figure 7 (b)), large variations exist due to the flexibility of anion and its small size. In the following section, this alteration of distance between CO<sub>2</sub> and anion is supported by the interaction energy data.

In addition to the structure difference in the bulk IL phase, the difference in gas-IL interface is also important, which is the origin of adsorption process. Therefore, density distributions of each gas and ion along the x-axis of IL systems are given in Figure 8 (a). Density distributions of cations and anions within the bulk ASF and OTF IL phases are comparably smoother than those within OAC and TFA IL phases, which supports the homogeneous distribution of ions, lack of localization of anion-cation pairs and, hence, lack of empty space where CO<sub>2</sub> can accommodate. However, although high adsorption capacity and large density variations of ions are observed for CO<sub>2</sub> in OAC and TFA, CO<sub>2</sub> density profile averaged from the ensemble of 15-ns simulation time displays that CO<sub>2</sub> concentration within IL phase is only observed for OAC. Since retention time of CO<sub>2</sub> within TFA IL phase is short, considerable density profile of CO<sub>2</sub> could not be calculated. On the other hand, ion distribution maps on the lateral surface of gas-IL interface are provided in Figure 8 (b) in order to visualize the surface porosity and gain insight about its effect on gas adsorption. More uniform distributions of ions are available on the surface of ASF and OAC gas-IL interfaces. However, there are several indentations on both surfaces of OTF and TFA gas-IL interfaces, which hinder the anion-cation network and, hence, eliminate the fast CO<sub>2</sub> adsorption. Probably, due to the fluorine groups, which hinder the rotation of anion, large cavities occurred on the surface of gas-IL interface of OTF and TFA systems. Collectively, coordination of anion around apolar tail of cation, anion-CO<sub>2</sub>-cation network, ratio of cation amount over anion surrounding CO<sub>2</sub>, and the surface porosity of gas-IL interface are the possible factors that are responsible for CO<sub>2</sub> adsorption capacity of IL and retention time within IL.

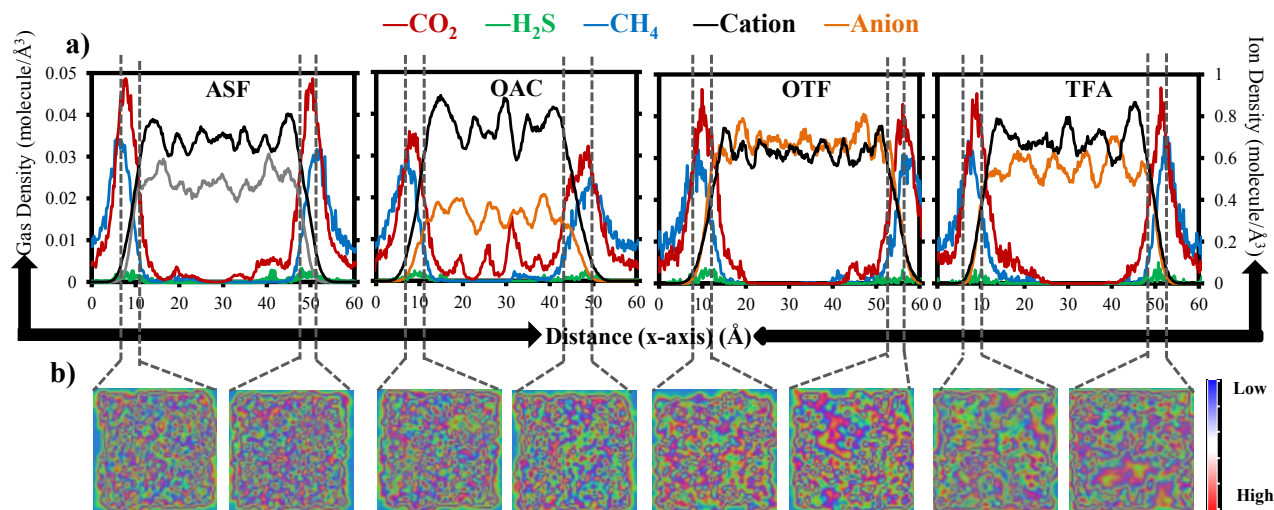


**Figure 8.** (a) Density profiles of  $\text{CO}_2$ ,  $\text{H}_2\text{S}$ ,  $\text{CH}_4$ , anion, and cation along x-axis observed by averaging over 15-ns simulation time. Please note that dashed grey lines represent the borders of gas-IL interfaces. Please note that from left to right, data belong to the ASF, OAC, OTF, and TFA, respectively. (b) 2D density maps of ions on the surface of gas-IL interfaces, where blue and red regions represent the low and high ion densities, respectively.

### 3.3. Interactions of ions with gases and within ion pairs

On top of qualitatively visualizing the different affinities between gases and ILs in Figure 6 (b) and Figure 7, it is worthwhile to further quantify the interactions especially, since the potential interaction energies between each pairs may have different contributions to the adsorption of gases. Accordingly, the average interaction energies of  $\text{H}_2\text{S}$ ,  $\text{CO}_2$ , and  $\text{CH}_4$  with cation and anion are quantified in Figures 9 (a-c), respectively. Cation molecule is the same in each IL and displays repulsive interaction energies with  $\text{H}_2\text{S}$  regardless of anion type. When average numbers of adsorbed  $\text{H}_2\text{S}$  molecules inside each IL bulk phase given in Figures 4 (a-d) are considered, highest and lowest values belong to ASF and TFA, respectively. Consistently, summation of average interaction energies of  $\text{H}_2\text{S}$ -anion and  $\text{H}_2\text{S}$ -cation pairs is greatest for ASF, which verifies its highest  $\text{H}_2\text{S}$  adsorption capacity. Similarly, low  $\text{H}_2\text{S}$  adsorption performance of TFA is related to low total interaction energy of  $\text{H}_2\text{S}$  with both anion and cation (Figure 9 (a)). In the same manner, the highest  $\text{CO}_2$  adsorption performance of OAC can be explained with the highest total interaction energy existing with anion and cation, respectively. Additionally, although  $\text{CO}_2$  adsorption capacity of TFA, and average interaction energy existing between  $\text{CO}_2$  and cation for TFA are also close to those of OAC,  $\text{CO}_2$  molecules cannot be trapped within IL phase and desorbed from other surface of IL. This is evidently due to the low average interaction energy between  $\text{CO}_2$  and anion (Figure 9 (b)), proving that synergy within anion- $\text{CO}_2$ -cation is very important for  $\text{CO}_2$  adsorption process in ILs. On the other hand, similar adsorption capacities of ILs for  $\text{CH}_4$  are verified with the almost same average interaction energies of  $\text{CH}_4$  with both cation and anion, as given in Figure 9 (c). Finally, when average interaction energies between cation and anion for all ILs are considered in Figure 9 (d),  $\text{CO}_2$  adsorption performances of IL are compatible with them, where OAC and TFA reveal the greater values. Collectively, while cation-anion interaction is critical for adsorption of  $\text{CO}_2$ , anion- $\text{CO}_2$  interaction is the responsible one for the retention of  $\text{CO}_2$  within IL phase. Total gas-ion interactions are more dominant for  $\text{H}_2\text{S}$ , which plays a role in the enhancement of  $\text{H}_2\text{S}/\text{CH}_4$  selectivity for ILs, especially for ASF.

Figure 10 presents the number of h-bonding between cation and anion molecules averaged over last 5 ns for each system including adsorbed gases within IL phase, which supports the findings of RDF provided in Figure 6. To understand the contribution of h-bonding to the average total interaction energy between anion and cation, average number of h-bonding analyses are performed based on the criteria provided in the “Computational Details” section, for some of specific sites in cation (see Figure 1 for atomic site labels) with oxygen in anions in Figures 10 (a-d). Average number of h-bonding between CW and anion is the least in all ILs, providing the negligible effect of CW in anion-cation interaction. While the highest numbers of h-bonding for OAC and TFA exist within the pairs of CR-anion and C1-anion, those for ASF and OTF belong to the pair of CT-anion. It is represented in Figures 6 (c) and 7 that considerable amounts of CT are present around  $\text{CO}_2$  molecules for each IL systems. However, as seen in Figures 10 (b) and 10 (d), number of h-bonding between CT and anion in OAC and TFA, which are the systems having high  $\text{CO}_2$  adsorption capacities, is much lower than those of CR-anion and C1-anion. This reveals that since CT atoms are not capable of creating high amount of

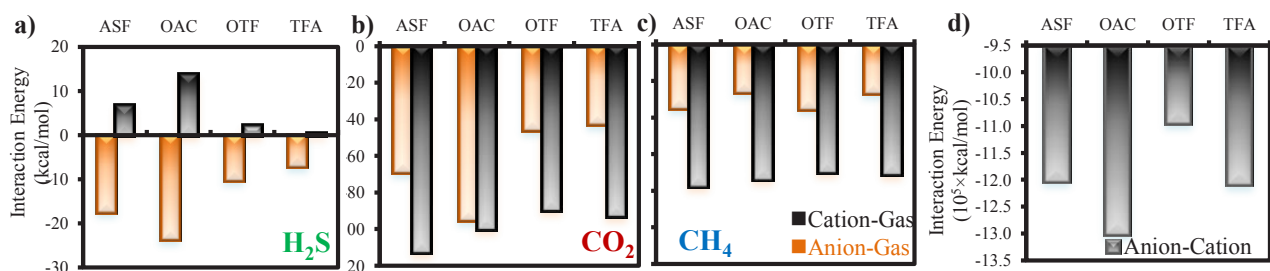


**Figure 9.** Average interaction energies over 15 ns between (a) anion–H<sub>2</sub>S, cation–H<sub>2</sub>S, (b) anion–CO<sub>2</sub>, cation–CO<sub>2</sub>, (c) anion–CH<sub>4</sub>, cation–CH<sub>4</sub>, and (d) anion–cation. Average interaction energies within gas–anion and gas–cation are represented in orange and black bars in (a – c).

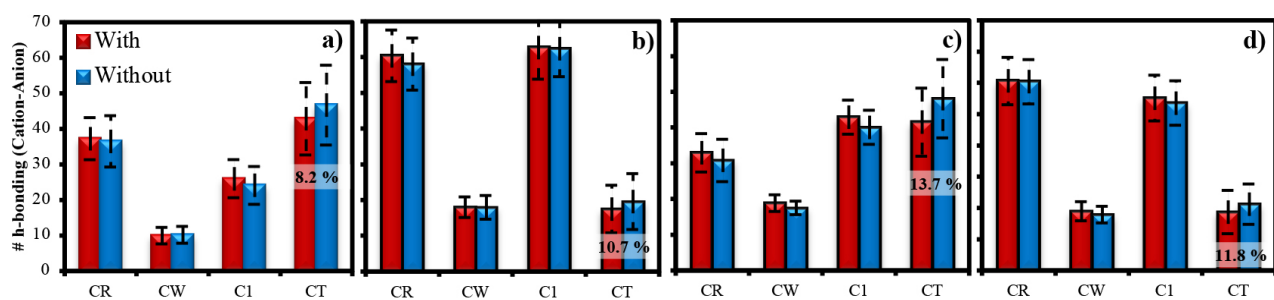


**Figure 10.** Average number of hydrogen bonding between specific groups (CR, CW, C1, CT) in cation and oxygen atoms in anion for (a) ASF, (b) OAC, (c) OTF, and (d) TFA ILs. Please see the investigated atomic sites in **Figure 1**, and note that error bars represent the standard deviation calculated in the last 5 ns of the production run when gases are present within IL (**with**), and in the final 2 ns of the production run when gases are absent within IL (**without**).

h-bonding with anions in OAC and TFA ILs, CO<sub>2</sub> can easily find a free space around the tail of cation (CT) and adsorbed there. However, it is worth to mention that the main interaction between anion and cation, which is governed by CR and C1 atoms in the head group of cation, manages the network of cation–CO<sub>2</sub>–anion. Additionally, while there are similar standard deviations (error bars) in the number of h-bonding of CT in OAC and TFA compared to the other sites in cation, those are much larger in ASF and OTF. Instabilities in the number of h-bonding of CT with anion in ASF and OTF reveal their weakness, although their number of h-bonding is high compared to other identified sites. On the other hand, when average number of h-bonding between ions of ILs with and without gas molecules are compared in Figure 10, it is seen that only an increase in the h-bonding number is observed for the CT–anion pair, regardless of IL system, while those of other pairs in all ILs either slightly decrease, or they are almost similar. Since CO<sub>2</sub> molecules prefer to locate between CT and anion, adsorption of CO<sub>2</sub> leads to the orientation of anions towards CT atoms (tail of cation), and hence this enables the increase in the number of h-bonding due to the localization as shown in Figure 7 (a). Collectively, although CT sites do not have considerable effect on the strength of anion–cation network, they manage the CO<sub>2</sub> adsorption by the help of h-bonding they created with anion.

#### 4. Conclusion

The development of effective adsorbent material for acidic gas separation is of paramount importance to ensure low acidic gas emissions. Therefore, in this study, novel adsorbent materials as ionic liquids are investigated using molecular simulation approaches. It is aimed to provide a detailed knowledge of H<sub>2</sub>S, CO<sub>2</sub>, and CH<sub>4</sub> adsorption capacities in gas-IL interface and bulk IL phase. Molecular dynamics simulations are used to reveal the adsorption mechanism of ASF, OAC, OTF, and TFA IL systems for acidic gases over 15 ns simulation time. Additionally, structural differences of each IL, their coordination around CO<sub>2</sub>, interaction between each pairs, and h-bonding between cation and anion are also identified for a detailed evaluation. OAC IL has the highest CO<sub>2</sub> adsorption capacity inside bulk IL phase as well as highest CO<sub>2</sub>/CH<sub>4</sub> adsorption selectivity compared to the rest of IL systems. However, greatest H<sub>2</sub>S/CH<sub>4</sub> adsorption selectivity belongs to the ASF due to the highest H<sub>2</sub>S adsorption aroused from the strong interactions of H<sub>2</sub>S with anions and cations. Since there are uniform distributions of ions on gas-IL interface of ASF and OAC systems, fast CO<sub>2</sub> adsorption is observed around 3 ns and fluctuate within the same value over the end of simulation time. On the other hand, although TFA reveals high

CO<sub>2</sub> adsorption capacity, it is not a prominent IL due to high CH<sub>4</sub> and low H<sub>2</sub>S adsorption capacity led to the decrease in selectivities, and short retention time of CO<sub>2</sub> inside IL bulk phase, which causes the adsorbed CO<sub>2</sub> molecules to desorb on the other surface of IL phase. More importantly, it is revealed that the interaction energy of anion-cation governs the CO<sub>2</sub> adsorption capacity by enabling anion-CO<sub>2</sub>-cation network. However, number of h-bonding between anion and cation should be less, so that the anion can be properly coordinated around the tail of cation to accommodate CO<sub>2</sub> within the free space available between them. The attained information/data can assist to develop and design suitable IL-based adsorbents for acidic gas adsorption.

### Conflict of interest

The author declares no competing financial interest.

### Acknowledgments

The numerical calculations reported in this paper were fully performed at TUBITAK (Scientific and Technological Research Council of Turkey) ULAKBIM, High Performance and Grid Computing Center (TRUBA resources).

### References

1. Hoegh-Guldberg O, Jacob D, Taylor M. IPCC special report. Volume 3: Global warming of 1.5°C on natural and human systems; 2018.
2. Bauer F, Persson T, Hulteberg C, Tamm D. Biogas upgrading-technology overview, comparison and perspectives for the future. *Biofuels Bioprod Biorefin* 2013; 7: 499-511. doi: 10.1002/bbb.1423
3. Costa Gomes M, Pison L, Červinka C, Padua A. Porous ionic liquids or liquid metal-organic frameworks? *Angewandte Chemie International Edition* 2018; 130 (37): 12085-12088. doi: 10.1002/anie.201805495
4. O'Reilly N, Giri N, James SL. Porous liquids. *Chemistry – A European Journal* 2007; 13 (11): 3020-3025. doi: 10.1002/chem.200700090
5. Mohamedali M, Ibrahim H, Henni A. Incorporation of acetate-based ionic liquids into a zeolitic imidazolate framework (ZIF-8) as efficient sorbents for carbon dioxide capture. *Chemical Engineering Journal* 2018; 334: 817-828. doi: 10.1016/j.cej.2017.10.104
6. Mohamedali M, Henni A, Ibrahim H. Markedly improved CO<sub>2</sub> uptake using imidazolium-based ionic liquids confined into HKUST-1 frameworks. *Microporous and Mesoporous Materials* 2019; 284: 98-110. doi: 10.1016/j.micromeso.2019.04.004
7. Shahrom MSR, Nordin AR, Wilfred CD. The improvement of activated carbon as CO<sub>2</sub> adsorbent with supported amine functionalized ionic liquids. *Journal of Environmental Chemical Engineering* 2019; 7 (5): 103319. doi: 10.1016/j.jece.2019.103319
8. Liu F, Huang K, Jiang L. Promoted adsorption of CO<sub>2</sub> on amine-impregnated adsorbents by functionalized ionic liquids. *AIChE Journal* 2018; 64 (10): 3671-3680. doi: 10.1002/aic.16333
9. Mallakpour S, Dinari M. Ionic liquids as green solvents: Progress and prospects. In *Green solvents II*, Springer: 2012; 1-32.
10. Blanchard L A, Hancu D, Beckman E J, Brennecke J F. Green processing using ionic liquids and CO<sub>2</sub>. *Nature* 1999; 399 (6731): 28-29. doi: 10.1038/19887
11. Aki SN, Mellein BR, Saurer EM, Brennecke JF. High-pressure phase behavior of carbon dioxide with imidazolium-based ionic liquids. *Journal of Physical Chemistry B* 2004; 108 (52): 20355-20365. doi: 10.1021/jp046895+
12. Shin E-K, Lee B-C. High-pressure phase behavior of carbon dioxide with ionic liquids: 1-alkyl-3-methylimidazolium trifluoromethanesulfonate. *Journal of Chemical and Engineering Data* 2008; 53 (12): 2728-2734. doi: 10.1021/jc8000443
13. Bara JE, Camper DE, Gin DL, Noble RD. Room-temperature ionic liquids and composite materials: platform technologies for CO<sub>2</sub> capture. *Accounts of Chemical Research* 2010; 43 (1): 152-159. doi: 10.1021/ar9001747
14. Huang X, Margulis CJ, Li Y, Berne BJ. Why is the partial molar volume of CO<sub>2</sub> so small when dissolved in a room temperature ionic liquid? Structure and dynamics of CO<sub>2</sub> dissolved in [Bmim][PF<sub>6</sub>]. *Journal of the American Chemical Society* 2005; 127 (50): 17842-17851. doi: 10.1021/ja055315z
15. Zhang X, Huo F, Liu Z, Wang W, Shi W et al. Absorption of CO<sub>2</sub> in the ionic liquid 1-n-hexyl-3-methylimidazolium tris (pentafluoroethyl) trifluorophosphate ([HMIM][FEP]): A molecular view by computer simulations. *Journal of Physical Chemistry B* 2009; 113 (21): 7591-7598. doi: 10.1021/jp900403q
16. Varma N R, Ramalingam A, Banerjee T. Experiments, correlations and COSMO-RS predictions for the extraction of benzothiophene from n-hexane using imidazolium-based ionic liquids. *Chemical Engineering Journal* 2011; 166 (1): 30-39. doi: 10.1016/j.cej.2010.09.015

17. Shiflett M B, Yokozeki A. Phase behavior of carbon dioxide in ionic liquids: [EMIM][Acetate], [EMIM][Trifluoroacetate], and [EMIM][Acetate] + [EMIM][Trifluoroacetate] mixtures. *Journal of Chemical and Engineering Data* 2009; 54 (1): 108-114. doi: 10.1021/jc800701j
18. Yokozeki A, Shiflett MB, Junk CP, Grieco LM, Foo T. Physical and chemical absorptions of carbon dioxide in room-temperature ionic liquids. *The Journal of Physical Chemistry B* 2008; 112 (51): 16654-16663. doi: 10.1021/jp805784u
19. Gómez-Coma L, Garea A, Irabien A. Non-dispersive absorption of CO<sub>2</sub> in [EMIM][EtSO<sub>4</sub>] and [EMIM][Ac]: Temperature influence. *Separation and Purification Technology* 2014; 132: 120-125. doi: 10.1016/j.seppur.2014.05.012
20. Mejía I, Stanley K, Canales R, Brennecke JF. On the high-pressure solubilities of carbon dioxide in several ionic liquids. *Journal of Chemical and Engineering Data* 2013; 58 (9): 2642-2653. doi: 10.1021/jc400542b
21. Zhang S, Chen Y, Ren R X-F, Zhang Y, Zhang J et al. Solubility of CO<sub>2</sub> in sulfonate ionic liquids at high pressure. *Journal of Chemical and Engineering Data* 2005; 50 (1): 230-233. doi: 10.1021/jc0497193
22. Shiflett MB, Niehaus AMS, Yokozeki A. Separation of CO<sub>2</sub> and H<sub>2</sub>S using room-temperature ionic liquid [BMIM][MeSO<sub>4</sub>]. *Journal of Chemical and Engineering Data* 2010; 55 (11): 4785-4793. doi: 10.1021/jc1004005
23. Ahmad MZ, Peters TA, Konnertz NM, Visser T, Téllez C et al. High-pressure CO<sub>2</sub>/CH<sub>4</sub> separation of Zr-MOFs based mixed matrix membranes. *Separation and Purification Technology* 2020; 230: 115858. doi: 10.1016/j.seppur.2019.115858
24. Liu L, Nicholson D, Bhatia SK. Adsorption of CH<sub>4</sub> and CH<sub>4</sub>/CO<sub>2</sub> mixtures in carbon nanotubes and disordered carbons: A molecular simulation study. *Chemical Engineering Science* 2015; 121: 268-278. doi: 10.1016/j.ces.2014.07.041
25. Plimpton S. Fast parallel algorithms for short-range molecular dynamics. *Journal of Computational Physics* 1995; 117 (1): 1-19. doi: 10.1006/jcph.1995.1039
26. Humphrey W, Dalke A, Schulten K. VMD: Visual molecular dynamics. *Journal of Molecular Graphics* 1996; 14 (1): 33-38. doi: 10.1016/0263-7855(96)00018-5
27. Kaminski GA, Friesner RA, Tirado-Rives J, Jorgensen WL. Evaluation and reparametrization of the OPLS-AA force field for proteins via comparison with accurate quantum chemical calculations on peptides. *The Journal of Physical Chemistry B* 2001; 105 (28): 6474-6487. doi: 10.1021/jp003919d
28. Canongia Lopes JN, Deschamps J, Pádua AA. Modeling ionic liquids using a systematic all-atom force field. *The Journal of Physical Chemistry B* 2004; 108 (6): 2038-2047. doi: 10.1021/jp0362133
29. Canongia Lopes JN, Pádua AA. Molecular force field for ionic liquids composed of triflate or bistriflylimide anions. *The Journal of Physical Chemistry B* 2004; 108 (43): 16893-16898. doi: 10.1021/jp0476545
30. Potoff JJ, Siepmann JI. Vapor-liquid equilibria of mixtures containing alkanes, carbon dioxide, and nitrogen. *Aiche J* 2001; 47 (7): 1676-1682.
31. Nath SK. Molecular simulation of vapor-liquid phase equilibria of hydrogen sulfide and its mixtures with alkanes. *The Journal of Physical Chemistry B* 2003; 107 (35): 9498-9504. doi: 10.1021/jp034140h
32. Martin MG, Siepmann JI. Transferable Potentials For Phase Equilibria. 1. United-Atom Description of N-Alkanes. *The Journal of Physical Chemistry B* 1998; 102 (14): 2569-2577.
33. Martínez L, Andrade R, Birgin EG, Martínez JM. PACKMOL: A package for building initial configurations for molecular dynamics simulations. *Journal of Computational Chemistry* 2009; 30 (13): 2157-2164. doi: 10.1002/jcc.21224
34. Doherty B, Zhong X, Gathiaka S, Li B, Acevedo O. Revisiting OPLS force field parameters for ionic liquid simulations. *Journal of Chemical Theory and Computation* 2017; 13 (12): 6131-6145. doi: 10.1021/acs.jctc.7b00520
35. Aghaie M, Rezaei N, Zendejboudi S. New insights into bulk and interface properties of [Bmim][Ac]/[Bmim][BF<sub>4</sub>] ionic liquid/CO<sub>2</sub> systems-Molecular dynamics simulation approach. *Journal of Molecular Liquids* 2020; 317: 113497. doi: 10.1016/j.molliq.2020.113497
36. Thomas A, Ahamed R, Prakash M. Selection of a suitable ZIF-8/ionic liquid (IL) based composite for selective CO<sub>2</sub> capture: The role of anions at the interface. *RSC Advances* 2020; 10 (64): 39160-39170. doi: 10.1039/d0ra07927h
37. Klahn M, Seduraman A. What determines CO<sub>2</sub> solubility in ionic liquids? A molecular simulation study. *The Journal of Physical Chemistry B* 2015; 119 (31): 10066-10078. doi: 10.1021/acs.jpcc.5b03674